Hydrology Research

British Hydrological Society

IWA PUBLISHING

Hydrology Research Vol 53 No 10, 1256 doi: 10.2166/nh.2022.021

A model for estimating the hydraulic conductivity of bentonite under various density conditions

Tatsuya Kijima[a,*], Tsuyoshi Sasagawa[b], Takuma Sawaguchi[b] and Norikazu Yamada[a]

[a] Regulatory Standard and Research Department, Secretariat of Nuclear Regulation Authority (S/NRA/R), 1-9-9, Roppongi, Minato-ku, Tokyo 106-8450, Japan
[b] Japan Atomic Energy Agency, 2-4, Shirakita, Tokai-mura, Naka-gun, Ibaraki 319-1195, Japan
*Corresponding author. E-mail: kijima_tatsuya_5mw@nra.go.jp

ABSTRACT

Bentonite is an important material for low-permeability engineering systems used in dams and hazardous waste facilities. While models to characterize the hydraulic conductivity of bentonite have been developed in previous studies, these models were not applicable to various density conditions for Na- and Ca-bentonite. In this study, we present a new model for estimating the hydraulic conductivity of bentonite applicable to a wide range of density conditions for Na- and Ca-bentonite. In order to consider flow paths in compacted bentonite, a lamination structure of montmorillonite stacks was assumed. Our hydraulic model discriminated interlayer pores and other pores by applying a method for estimating the probability of connected pores and hydraulic coefficients governed by the plane Poiseuille flow equation. The model was consistent with the experimental data investigated in previous studies on the hydraulic conductivity of Na-bentonite and was in good agreement with the data of Ca-bentonite in the range of an effective montmorillonite density (ρ_{em}) at 500 kg/m^3 $\leq \rho_{em} \leq$ 1,500 kg/m^3 and 600 kg/m^3 $\leq \rho_{em}$, respectively. However, some experimental values on Ca-bentonite under low-density conditions were far higher than the model results in the case where Ca-bentonite forms flow paths of relatively large pores.

Key words: bentonite, hydraulic conductivity, hydraulic model, montmorillonite

HIGHLIGHTS

- A model for estimating the hydraulic conductivity of bentonite was proposed.
- The model discriminated interlayer pores from other pores in the bentonite.
- The relation between a wide range of effective montmorillonite densities and basal spacings for Na-montmorillonite was proposed.

INTRODUCTION

Low-permeability clay soil is a key material for water control systems, and hydraulic conductivity is a significant factor to evaluate the system. Low hydraulic conductivity soils ensure the safety of drinking water in the natural system (Nahin *et al.* 2019) and are used for groundwater control in engineering systems such as dams and hazardous waste facilities (Gueddouda *et al.* 2016; Park & Oh 2018; Santos & Esquivel 2018). Bentonite, which is a representative material for engineering systems, uses as clay liners and backfills for hazardous waste facilities and cutoff walls for earth dams, and is a suitable material to prevent groundwater flow and migration of hazardous materials (i.e., heavy metals and radionuclides) (Meer & Benson 2007; Malusis *et al.* 2011). Montmorillonite, a major component of bentonite clay, plays a role in this function via a filling of the bentonite pores through its swelling property. Compacted bentonite and sand-bentonite mixtures are used in engineering systems when suitable for the performance required (Lee & Shackelford 2005; Gueddouda *et al.* 2016).

Many experiments for determining the hydraulic conductivities of bentonite and montmorillonite have been conducted for using as an engineered barrier in radioactive waste disposal facilities (e.g., Suzuki *et al.* 1992; Matsumoto *et al.* 1997; Maeda *et al.* 1998). Some experiments have revealed that compacted bentonite and montmorillonite saturated with water are composed of stacking laminations of several montmorillonite particles (Pusch *et al.* 1990). Other studies have found that the water flowing near the montmorillonite surface has a higher viscosity than bulk water due to an effect of the surface charge of montmorillonite (Low 1976; Maeda *et al.* 1998; Ichikawa *et al.* 1999). Based on these experimental results,

models for estimating the hydraulic conductivity of bentonite have been proposed. Komine (2008) considered two montmorillonite particles as a base unit and proposed a flow of water through their interval; however, they did not distinguish the interlayer pores of the montmorillonite from the other pores (hereinafter defined as external pores) and neglected to perform any quantitative analysis of the viscosity change of water. Since the width of the interlayer pore differs from that of the external pore, the hydraulic conductivities in the interlayer and the external pore also differ. The same problems arose when the Kozeny–Carman relation was applied to bentonite and montmorillonite (Ren *et al.* 2016; Kobayashi *et al.* 2017; Kohno 2021). Tanaka *et al.* (2009) proposed a model for hydraulic conductivity estimation that distinguished between interlayer pores and external pores. Their model, however, focused on high-effective montmorillonite density (the montmorillonite weight divided by the sum of the volumes of pores and montmorillonite) conditions and thus could not be applied under low-density conditions.

The previously proposed models also have the problem of not employing generalized equations for application to a wide range of effective montmorillonite densities. The interlayer pore width of montmorillonite changes in accordance with variations in the interlayer cation, water content, and ionic strength of the solution (Foster *et al.* 1954; Norrish 1954; Fink & Thomas 1964; Fukushima 1984; Zhang & Low 1989). The relation between the interlayer pore width and water content has been parameterized by the effective montmorillonite density of Na- and Ca-montmorillonite. Although the relations under high-effective montmorillonite density conditions (over 800 kg/m^3) have been obtained (Kozaki *et al.* 1998; Suzuki *et al.* 2001; Wang *et al.* 2021), those under low-effective montmorillonite density conditions have been insufficient. The relation under low-effective montmorillonite density conditions is significant because sand-bentonite mixtures containing 10–30% bentonite have the potential to be used in low-level radioactive waste disposal facilities and other engineering systems. The difference between Na- and Ca-bentonite is important to evaluate the hydraulic performance of the clay liner used in hazardous waste facilities because their permeabilities are quite different when the bentonite content is low (Maeda *et al.* 1998). However, the estimation method of the hydraulic conductivities considering the water flow paths in bentonite for both Na- and Ca-type of various bentonite content is insufficient.

The objectives of this study are to evaluate the relation among the interlayer pore, external pore width, and effective montmorillonite density, and to develop a model to estimate the hydraulic conductivity of both Na- and Ca-bentonite under the wide range of effective montmorillonite densities based on this relation.

ESTIMATION OF THE POROSITY OF EXTERNAL PORES AND INTERLAYER PORES

A schematic image of a montmorillonite particle, stack, interlayer pore, and external pore is shown in Figure 1. The porosities of these two pores are calculated as outlined below, assuming that the montmorillonite particle shape is cylindrical. A volume

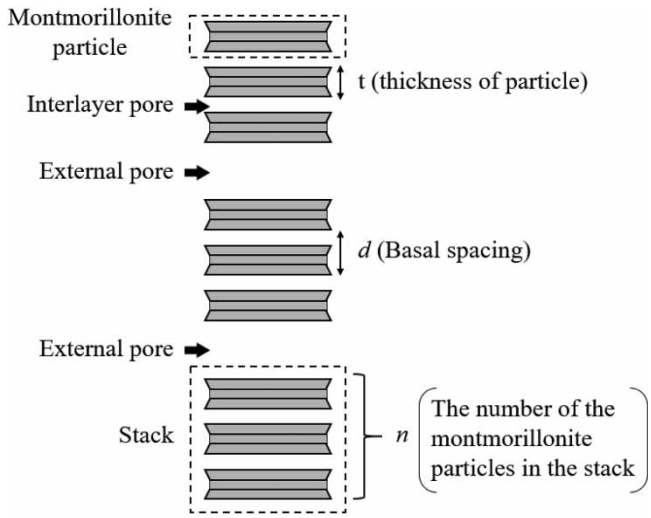

Figure 1 | Schematic image of a montmorillonite particle, stack, interlayer pore, and external pore.

of the stack is expressed as follows:

$$V = \pi R^2 \cdot [n \cdot t + (n-1) \cdot (d-t)] \tag{1}$$

where V is the volume of the stack (m^3), R is the radius of the montmorillonite particle (m), n is the number of montmorillonite particles in the stack (–), t is the thickness of the montmorillonite particle (m), and d is the basal spacing (m).

The weight of the montmorillonite particle is expressed as follows:

$$m = \pi R^2 t \rho_m \tag{2}$$

where m is the weight of the montmorillonite particle (kg), and ρ_m is the particle density of the montmorillonite (kg/m^3).

Assuming that the compacted montmorillonite specimen is a cube of the length H (m), the weight of the montmorillonite in the specimen is expressed as follows:

$$M_m = \rho_{em} H^3 \tag{3}$$

where M_m is the weight of the montmorillonite in the specimen (kg), ρ_{em} is the effective montmorillonite density (representing bulk density when the specimen is composed of only montmorillonite) (kg/m^3), and H is the length of the specimen (m).

The number of stacks in the specimen is expressed as follows:

$$N = M_m/(n \cdot m) \tag{4}$$

where N is the number of the stacks in the specimen (–).

The total volume of the stacks in the specimen (V_t), the total volume of the external pores in the specimen (V_{ext}), and the total volume of the interlayer pores in the specimen (V_{int}) are expressed by the following equations.

$$V_t = N \cdot V \tag{5}$$

$$V_{ext} = H^3 - V_t \tag{6}$$

$$V_{int} = N \cdot \pi R^2 \cdot (n-1) \cdot (d-t) = \frac{V_t}{V} \cdot \pi R^2 \cdot (n-1) \cdot (d-t) = V_t - \pi R^2 \cdot n \cdot N \cdot t \tag{7}$$

An external pore porosity (ε_{ext}) and an interlayer pore porosity (ε_{int}) are expressed as follows:

$$\varepsilon_{ext} = \frac{V_{ext}}{V_t + V_{ext}} = 1 - \frac{\rho_{em}}{\rho_m}\left\{1 + \frac{(n-1)(d-t)}{nt}\right\} \tag{8}$$

$$\varepsilon_{int} = \frac{V_{int}}{V_t + V_{ext}} = \frac{\rho_{em}}{\rho_m}\frac{(n-1)(d-t)}{nt} \tag{9}$$

The number of particles in a single stack and the basal spacing are necessary to solve Equations (8) and (9). X-ray diffraction (XRD) revealed the relations between the water content and basal spacing for a Na-montmorillonite suspension (Foster *et al.* 1954; Norrish 1954; Fink & Thomas 1964; Zhang & Low 1989) and the relations between the effective montmorillonite density (ρ_{em}) and basal spacing (d) for a compacted Na-montmorillonite (Kozaki *et al.* 1998; Suzuki *et al.* 2001; Holmboe *et al.* 2012). Kozaki *et al.* (1998) observed the basal spacing of a three-water-layer hydrate state (3WH state, $d = 1.88$ nm) and a two-water-layer hydrate state (2WH state, $d = 1.56$ nm) for compacted bentonite. The reported values of the effective montmorillonite density (ρ_{em}) corresponding to the 3WH state alone were $1{,}000\ kg/m^3 < \rho_{em} \leq 1{,}300\ kg/m^3$, to a mixed state of the 3WH state and 2WH state were $1{,}300\ kg/m^3 < \rho_{em} < 1{,}600\ kg/m^3$, and to the 2WH state alone were $1{,}600\ kg/m^3 \leq \rho_{em}$. Additionally, Suzuki *et al.* (2001) observed the basal spacing of a mixed state of $d = 3.52$ nm and a 3WH state. The reported ρ_{em} values corresponding to the mixed state were $800\ kg/m^3 \leq \rho_{em} \leq 1{,}000\ kg/m^3$. While these former reports determined the hydrate states by assessing whether the diffraction peaks of the basal spacing appeared, Holmboe *et al.* (2012) determined the hydrate states based on the peak ratio using data fitting to the diffraction peaks. While the hydration states at $1{,}300\ kg/m^3 < \rho_{em}$

were in agreement with the reports of Kozaki *et al.* (1998) and Suzuki *et al.* (2001), those at $\rho_{em} \leq 1{,}300$ kg/m^3 were not. Holmboe *et al.* (2012) determined that the hydration states at $\rho_{em} \leq 1{,}300$ kg/m^3 were a mixed state of crystalline swelling (stepwise expansion) and osmotic swelling (continuous expansion), and did not observe a clear diffraction peak resulting from the 3WH state at $\rho_{em} = 1{,}000$ kg/m^3. In contrast, Kozaki *et al.* (1998) and Suzuki *et al.* (2001) observed this peak at the same density. Holmboe *et al.* (2012) explained this difference by the effects of the water content without using any profile fitting or the particle size. The degree of difference of the basal spacing reported by Kozaki *et al.* (1998) and Holmboe *et al.* (2012), however, was only about 0.1 nm, and a value assumed not to be significantly different in the estimation of the hydraulic conductivity because the change in the hydraulic conductivities would be order of 3% based on our proposed model.

As any studies have hardly shown the relation between the basal spacing and the effective montmorillonite density at 800 kg/m^3 $< \rho_{em}$ (Holmboe *et al.* 2012), this relation was calculated from the relation between the water content (w) and the basal spacing under an assumed condition of water saturation.

$$w = \frac{M_w}{M_m} = \frac{\left(1 - \dfrac{\rho_{em}}{\rho_m}\right)\rho_w}{\rho_{em}}$$

$$\rho_{em} = \frac{\rho_w \cdot \rho_m}{\rho_w + w \cdot \rho_m} \tag{10}$$

where w is the water content (–), M_w is the weight of water in the specimen, and ρ_w is the water density (kg/m^3).

The relation between the basal spacing and the effective montmorillonite density calculated from Equation (10) using the previous experimental water content data (Foster *et al.* 1954; Norrish 1954; Fink & Thomas 1964; Zhang & Low 1989; Holmboe *et al.* 2012) is shown in Figure 2. The osmotic swelling occurred at $\rho_{em} \leq 900$ kg/m^3 and the crystalline swelling occurred at 700 kg/m^3 $\leq \rho_{em}$. The density conditions of the osmotic and crystalline swelling determined by the montmorillonite suspension were consistent with the results for the compacted montmorillonite, whose density was 800 kg/m^3 $\leq \rho_{em} \leq$ 1,000 kg/m^3 with a mixed state of osmotic and crystalline swelling (Kozaki *et al.* 1998; Suzuki *et al.* 2001). It is an important point that Figure 2 shows a continuous decreasing of basal spacing as increasing density at $\rho_{em} <$ 1,000 kg/m^3. Figure 2 also shows that d values for the crystalline swelling, $d = 1.88$ nm, 1.56 nm, and mixed state of them, are consistent with the results for the compacted montmorillonite, whose density is 1,000 kg/m^3 $< \rho_{em}$ (Kozaki *et al.* 1998). The values of the effective montmorillonite density (ρ_{em}) corresponding to the basal spacing affected by the osmotic swelling alone were determined as $\rho_{em} <$ 700 kg/m^3, those affected by the mixed state of osmotic and crystalline swelling were determined as 700 kg/m^3 $\leq \rho_{em} <$ 1,000 kg/m^3, and those affected by the crystalline swelling alone were determined as 1,000 kg/m^3 $\leq \rho_{em}$, for

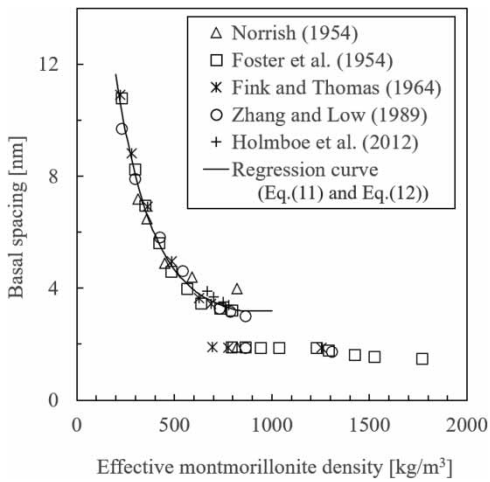

Figure 2 | Relation between the effective montmorillonite density and basal spacing for Na-montmorillonite.

Na-montmorillonite. A regression curve of the basal spacing for osmotic swelling is determined by the following equations.

$$\text{For } d > 3.2\,\text{nm}, \quad 1,000\,\text{kg/m}^3 \geq \rho_{em}$$

$$d = 25.41\exp(-0.005334\rho_{em}) + 2.898 \tag{11}$$

In the case of the result of the d-value calculated by using Equation (11) less than or equal to 3.2 nm.

$$d = 3.2 \tag{12}$$

The basal spacing jumped from 1.88 to 3.2–4.1 nm (Norrish 1954; Fukushima 1984; Zhang & Low 1989; Suzuki *et al.* 2001). We assumed that the basal spacing jumped from 1.88 to 3.2 nm (Zhang & Low 1989), and that the basal spacing was osmotic swelling as determined by Equations (11) and (12). As noted above, the difference in the basal spacing of 0.1 nm assumed not to be significantly different in the estimation of the hydraulic conductivity.

Although the swelling behavior of Ca-montmorillonite is the same as that of Na-montmorillonite at 1,000 kg/m$^3 \leq \rho_{em}$, the 3WH state supplants osmotic swelling as the dominant state at lower-density conditions (Fukushima 1984; Matusewicz *et al.* 2013). Therefore, the basal spacing of crystalline swelling is reasonable under all density conditions for Ca-montmorillonite.

LAMINATED ANGLES OF STACKS UNDER A COMPACTED CONDITION

X-ray CT observations of compacted montmorillonite showed that the montmorillonite particles were oriented perpendicularly to the direction of compaction (Takahashi & Tachi 2019). Diffusion tests using tritiated water (HTO) also revealed that the effective diffusivities for compacted montmorillonite changed according to the direction of diffusion (axial and perpendicular directions to compaction) (Sato & Suzuki 2003; Suzuki *et al.* 2004). The effective diffusivity is expressed as follows (Tachi & Yotsuji 2014):

$$De_i = \varepsilon_{total} \cdot G \cdot Dw_i \tag{13}$$

$$G = \delta_g \delta_{el} / \tau^2 \tag{14}$$

where De_i is the effective diffusivity of species i (m^2/s), ε_{total} is the total porosity (–), Dw_i is the diffusivity of species i in bulk water (m^2/s), G is a geometric factor (–), δ_g is the geometric constrictivity (–), δ_{el} is the electric constrictivity (–), and τ is the tortuosity (–).

The geometric constrictivity and electric constrictivity depend on the pore shape and the electrostatic interactions with a negatively charged clay surface, respectively. The tortuosity represents an actual diffusion path length relative to the specimen length. From the viewpoint of the diffusional direction, the pore shape and the electrostatic interactions do not affect the differences in the effective diffusivities of HTO. Therefore, the effective diffusivity of HTO is affected by only the diffusion path length. Figure 3 shows a schematic image of the diffusion path lengths when the stacks laminate with an average angle θ. The symbols $\theta_{a,y}$ and $\theta_{p,x}$ represent the lamination angles of the stack in axial and perpendicular directions to compaction, respectively (x and y are any positive integer). The average angles of $\theta_{a,y}$ and $\theta_{p,x}$ are equal to θ. $L_{a,y}$ and $L_{p,x}$ represent the diffusion path lengths in the axial and perpendicular directions to compaction per stack, respectively. The total lengths of $L_{a,y}$ and $L_{p,x}$ are equal to L_a and L_p, respectively. Assuming this laminated condition, the diffusion path lengths for the axial and perpendicular directions to compaction are given as follows:

$$L_a = \sum_{y=1} L_{a,y} = H/\sin\theta \tag{15}$$

$$L_p = \sum_{x=1} L_{a,x} = H/\cos\theta \tag{16}$$

where L_a is the diffusion path length axial to the compaction (m) and L_p is the diffusion path length perpendicular to the compaction (m).

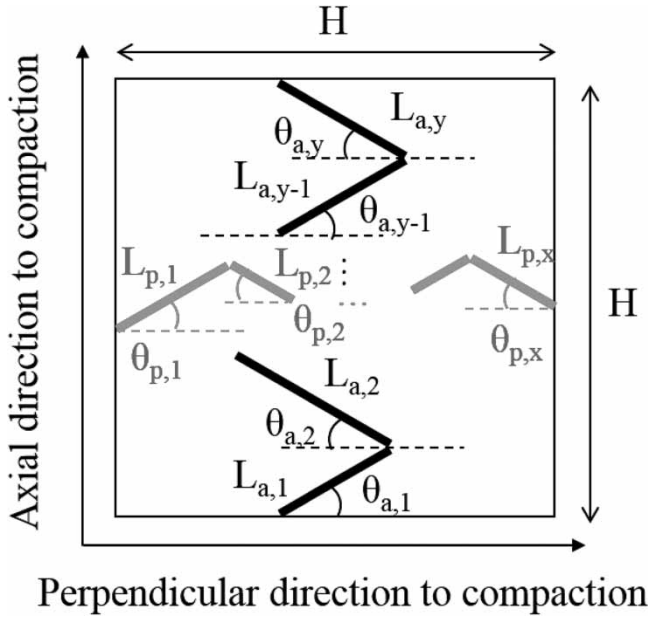

Figure 3 | Schematic image of path lengths.

The relation between the effective diffusivity ratio of the diffusional direction of HTO and the average laminated angle of stacks is calculated from Equations (13)–(16).

$$\frac{De_{HTO,p}}{De_{HTO,a}} = \left(\frac{\tau_a}{\tau_p}\right)^2 = \left(\frac{L_a/H}{L_p/H}\right)^2 = \left(\frac{\cos\theta}{\sin\theta}\right)^2 \tag{17}$$

where $De_{HTO,p}$ and $De_{HTO,a}$ are the effective diffusivity of HTO for the perpendicular and axial directions to compaction, respectively (m^2/s), and τ_p and τ_a represent the tortuosity perpendicular to and along the axial direction of compaction, respectively (–).

Figure 4 shows the relation between the effective montmorillonite density and the average laminated angles of the stacks. The average laminated angles of the stacks were calculated from the effective diffusivities from previous studies (Sato & Suzuki 2003; Suzuki *et al.* 2004). The effective montmorillonite density increases as the average laminated angle tends to decrease. The average laminated angles at arbitrary densities are obtained by least-squares regression (Equation (18)).

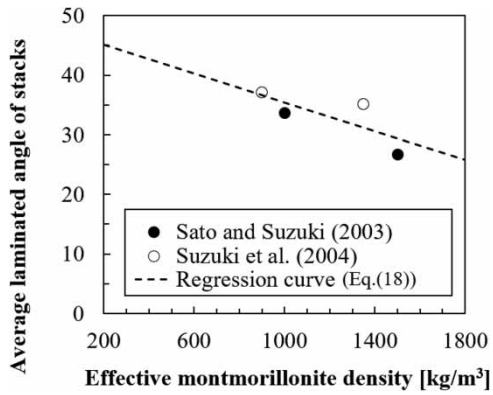

Figure 4 | Relation between the effective montmorillonite density and the averaged laminated angle of stacks calculated from the effective diffusivity of Sato & Suzuki (2003) and Suzuki *et al.* (2004).

Since the range of effective montmorillonite densities of the effective diffusivity is narrow due to the limited data, the average laminated angles out of this range are obtained by extrapolation of the regression line.

$$\theta = -0.01206\rho_{em} + 47.48 \tag{18}$$

$$R^2_{det} = 1 - \frac{RSS}{TSS} \tag{19}$$

where R^2_{det} is the coefficient of determination, RSS is the residual sum of squares, and TSS is the total sum of squares.

The coefficient of determination ($R^2 = 0.58$) is reasonably good. The average laminated angles of the stacks calculated from Sato & Suzuki (2003) are lower values than those calculated from Suzuki *et al.* (2004). High ionic strength solutions (0.55 and 1.1 M) were used in diffusion tests by Sato & Suzuki (2003), while pure water was used in them by Suzuki *et al.* (2004). It is possible that the difference of ionic strength affects the average laminated angles of the stacks, but we cannot explain moreover about this because the usable data are limited.

On the other hand, the effective diffusivity of HTO showed no changes in response to shifts in the diffusional directions for the bentonite and sand-bentonite mixtures because of containing minerals other than montmorillonite (Sato & Suzuki 2003). An average laminated angle of 45° was therefore selected for this study, as the montmorillonite particles do not appear to orient in a particular direction in the bentonite and sand-bentonite mixtures.

EVALUATION OF THE WIDTHS OF THE EXTERNAL PORES AND INTERLAYER PORES

Based on the previous studies (Komine 2008; Iida *et al.* 2011), hydraulic conductivities were modeled, assuming that each stack was a parallel plate. Some studies (Bolt 1956; Sidharan & Choudhury 2008) obtained the relation between the pore width of parallel clay plates and the void ratio, but they did so without assuming different widths for the external and interlayer pores. In the present study, we estimated the hydraulic conductivities of water flowing through both interlayer pores and external pores, with the assumption that the pore widths differed. As mentioned above, the external pore width is calculated from the stacks of n layers of particles. The relation between the void ratio contributed by the external pores and the external pore width is given as follows:

$$e_{ext} = \frac{V_{ext}}{V_t} = \frac{\dfrac{m \cdot n \cdot N}{\rho_{em}} - N \cdot V}{N \cdot V} = \frac{m \cdot n - \rho_{em} \cdot V}{\rho_{em} \cdot V} \approx \frac{m \cdot n \cdot S_{ext} \cdot A_{ext}}{V} - \frac{2A_{ext}}{R} \tag{20}$$

where e_{ext} is the void ratio contributed by the external pores (–), S_{ext} is a specific surface area of the stack ($\mathrm{m^2/kg}$), and A_{ext} is a half distance of the width of the external pore (m).

The interlayer pore width of the osmotic swelling is calculated from a regression curve (Equations (11) and (12)) in Figure 2 plotting the relation between the effective montmorillonite density and basal spacing. The basal spacing of the mixed state of the osmotic and crystalline swelling was at $700\ \mathrm{kg/m^3} \le \rho_{em} < 1{,}000\ \mathrm{kg/m^3}$ for Na-montmorillonite. As the abundance ratio of the number of stacks attributed to the osmotic or crystalline swelling was difficult to evaluate precisely, we assumed that the osmotic swelling stacks had an abundance ratio of 100% at $\rho_{em} = 700\ \mathrm{kg/m^3}$ and 0% at $\rho_{em} = 1{,}000\ \mathrm{kg/m^3}$, and *vice versa* for the crystalline swelling. The abundance ratio of the stacks between these densities was calculated from linear interpolation. The basal spacing of the mixed state consisting of the 3WH and 2WH states was estimated at $1{,}300\ \mathrm{kg/m^3} < \rho_{em} < 1{,}600\ \mathrm{kg/m^3}$ for Na-montmorillonite and Ca-montmorillonite. We assumed that the stacks had an abundance ratio of 100% at $\rho_{em} = 1{,}300\ \mathrm{kg/m^3}$ and 0% at $\rho_{em} = 1{,}600\ \mathrm{kg/m^3}$ for the 3WH state, and *vice versa* for the 2WH state. Between these densities, the abundance ratio of the stacks was calculated in the same manner used for Na-montmorillonite at $700\ \mathrm{kg/m^3} \le \rho_{em} < 1{,}000\ \mathrm{kg/m^3}$. The external pore width was calculated by Equations (1), (11), (12), and (20) using the calculation parameters as shown in Table 1. The external pore width decreases as the effective montmorillonite density increases, and also as the number of laminations in the stack (n) decreases (Figure 5). If the number of laminations exceeds 4 for Na-montmorillonite, the external pore width at $\rho_{em} = 1{,}000\ \mathrm{kg/m^3}$ is larger than that at $\rho_{em} = 700\ \mathrm{kg/m^3}$, based on the assumed ratio of the osmotic swelling to the 3WH states. Having a large external pore width implies that the specimen has enough space for montmorillonite swelling. Since only crystalline swelling was observed at $\rho_{em} = 1{,}000\ \mathrm{kg/m^3}$ (Kozaki *et al.* 1998), it would be unreasonable to assume that the external pore width at $\rho_{em} = 1{,}000\ \mathrm{kg/m^3}$ is larger than

Table 1 | Properties of montmorillonite particle

Diameter of montmorillonite particle (2R)	3.91×10^{-7} [m] (Suzuki *et al.* 2012)
Thickness of montmorillonite particle (t)	9.55×10^{-10} [m] (Tournassat *et al.* 2003)
Particle density of montmorillonite (ρ_m)	2,770 (kg/m^3) (Komine 2008)

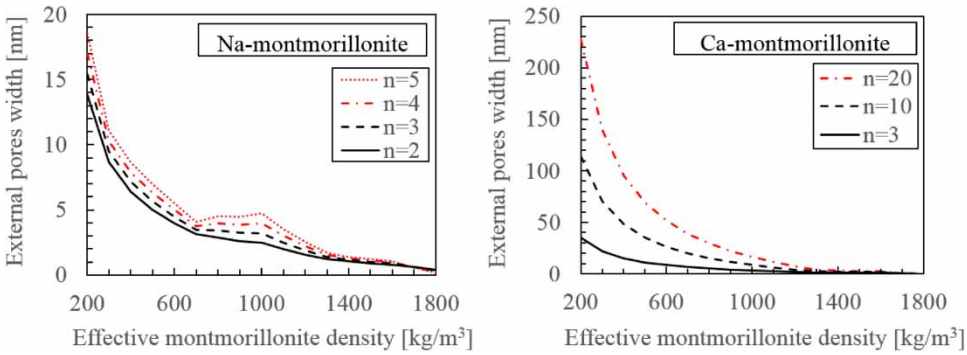

Figure 5 | Relation between effective montmorillonite density and external pore width (n represents the number of laminations in a single stack).

that at $\rho_{em} = 700$ kg/m^3. In contrast to the unreasonable behavior observed for Na-montmorillonite with an n over 3, the external pore width in the case of Ca-montmorillonite decreases monotonically as the effective montmorillonite density increases in every lamination number. This difference between Na-montmorillonite and Ca-montmorillonite was due to the difference in their swelling behavior. Although Na-montmorillonite could form the osmotic state (the d-value was over 3.2 nm) under any effective montmorillonite density condition other than 1,000 kg/m$^3 \leq \rho_{em}$, Ca-montmorillonite could swell only up to the 3WH state (the d-value was 1.88 nm) under the density condition of $\rho_{em} <$ 1,000 kg/m^3. Therefore, we determined that the number of laminations for Na-montmorillonite was 2 and 3, while that for Ca-montmorillonite was an arbitrary number above 2.

EVALUATION OF HYDRAULIC CONDUCTIVITY

The hydraulic conductivities of compacted montmorillonite and bentonite are estimated by assuming a plane Poiseuille flow in the external and interlayer pores. Hydraulic paths are presumed to compose complicatedly by the coupling of the external and interlayer pores. Based on the probability of connected pores at arbitrary adjacent cross-sections (Childs & Collis-George 1950; Marshall 1958; Millington & Quirk 1961), this study follows the method of Millington & Quirk (1961) and uses coefficients of a plane Poiseuille flow (Komine 2008) (M&Q model). The relation between the hydraulic conductivity and probability of connected pores at arbitrary adjacent cross-sections is given as follows:

$$k_{M\&Q} = \frac{\rho_w g}{12\mu} (\varepsilon_{total})^{4/3} \sum_j \sum_k X_{j,k}^2 f(X_j) f(X_k) \tag{21}$$

where $k_{M\&Q}$ is the hydraulic conductivity (m/s), g is the gravitational acceleration (m/s^2), μ is the viscosity of water (Pa·s), $X_{j,k}$ is the smaller width of X_j and X_k (m), and $f(X_j)$ and $f(X_k)$ are probabilities of the presence of the pore widths of X_j or X_k in the arbitrary cross-sections (–).

An apparent hydraulic gradient is calculated by dividing a pressure difference between the upper and lower ends of the specimen by the specimen length. Since the hydraulic paths are longer than the specimen length, as mentioned before, however, the actual hydraulic gradient in the pores is smaller than the apparent hydraulic gradient. A relation between the apparent hydraulic gradient (I_{app}) and the actual hydraulic gradient in the pores (I) can be expressed using the average

laminated angle of the stacks (θ) (Tanaka *et al.* 2009):

$$I_{app} = \frac{1}{\rho_w g}\left(\frac{\partial p}{\partial z}\right) = \frac{1}{\rho_w g}\frac{\Delta p}{H} = \frac{1}{\rho_w g}\frac{\Delta p}{L_a \sin\theta} = \frac{I}{\sin\theta} \tag{22}$$

where $\partial p/\partial z$ is the pressure gradient in the flow direction (Pa/m), and Δp is the pressure difference between the upper and lower ends of the specimen (Pa).

As Equation (21) does not consider the difference between the actual hydraulic gradient and the apparent hydraulic gradient in the pores, the apparent hydraulic conductivity for the specimen is expressed as follows:

$$\begin{aligned} k_{M\&Q,app} &= \frac{\rho_w g}{12\mu}(\varepsilon_{total})^{4/3}\sum_j\sum_k X_{jk}^2 f(X_j) f(X_k)\cdot\sin\theta \\ &= \frac{\rho_w g}{3\mu}(\varepsilon_{total})^{4/3}\left[A_{2WH}^2\left(\frac{\varepsilon_{2WH}}{\varepsilon_{total}}\right)^2 + A_{3WH}^2\left(\frac{\varepsilon_{3WH}}{\varepsilon_{total}}\right)^2 + A_{osm}^2\left(\frac{\varepsilon_{osm}}{\varepsilon_{total}}\right)^2 + A_{ext}^2\left(\frac{\varepsilon_{ext}}{\varepsilon_{total}}\right)^2 + 2\left\{A_{2WH}^2\left(\frac{\varepsilon_{2WH}}{\varepsilon_{total}}\right)\left(\frac{\varepsilon_{3WH}}{\varepsilon_{total}}\right)\right.\right. \\ &\left.\left. + X_{2WH,ext}^2\left(\frac{\varepsilon_{2WH}}{\varepsilon_{total}}\right)\left(\frac{\varepsilon_{ext}}{\varepsilon_{total}}\right) + A_{3WH}^2\left(\frac{\varepsilon_{3WH}}{\varepsilon_{total}}\right)\left(\frac{\varepsilon_{osm}}{\varepsilon_{total}}\right) + X_{3WH,ext}^2\left(\frac{\varepsilon_{3WH}}{\varepsilon_{total}}\right)\left(\frac{\varepsilon_{ext}}{\varepsilon_{total}}\right) + X_{osm,ext}^2\left(\frac{\varepsilon_{osm}}{\varepsilon_{total}}\right)\left(\frac{\varepsilon_{ext}}{\varepsilon_{total}}\right)\right\}\right]\cdot\sin\theta \end{aligned} \tag{23}$$

where A is the half distance of pore width (m); the subscripts *2WH*, *3WH*, and *osm* stand for the interlayer pores of the 2WH state, 3WH state, and osmotic swelling state, respectively; and the subscript *ext* stands for the external pore.

To clarify the effect of the pore connections, we examine extreme cases where the external pores and interlayer pores are assumed to be independent of each other (parallel model) and the pore connections are assumed to be completely random (series model). The apparent hydraulic conductivities for the parallel and series model are expressed as follows:

Parallel model

$$\begin{aligned} k_{p,app} &= \frac{\rho_w g}{12\mu}\cdot\sum_i X_i^2\cdot\varepsilon_i\cdot\sin\theta \\ &= \frac{\rho_w g}{3\mu}\{A_{2WH}^2\cdot\varepsilon_{2WH} + A_{3WH}^2\cdot\varepsilon_{3WH} + A_{osm}^2\cdot\varepsilon_{osm} + A_{ext}^2\cdot\varepsilon_{ext}\}\cdot\sin\theta, \end{aligned} \tag{24}$$

Series model

$$\begin{aligned} k_{s,app} &= \frac{\varepsilon_{total}^2}{\frac{12\mu}{\rho_w g}\sum_i\frac{\varepsilon_i}{X_i^2}}\cdot\sin\theta \\ &= \frac{\varepsilon_{total}^2}{\frac{3\mu}{\rho_w g}\left\{\frac{\varepsilon_{2WH}}{A_{2WH}^2} + \frac{\varepsilon_{3WH}}{A_{3WH}^2} + \frac{\varepsilon_{osm}}{A_{osm}^2} + \frac{\varepsilon_{ext}}{A_{ext}^2}\right\}}\cdot\sin\theta, \end{aligned} \tag{25}$$

where ε_i is the porosity contributed by pore i (–).

The viscosity of water in the pores affected by the surface charge of montmorillonite is expressed as follows (Andrade & Dodd 1946):

$$\frac{1}{\mu(x)} = \frac{1}{X_i}\int_0^{X_i}\frac{1}{\mu_0\left[1 + f_{ve}\left(\frac{d\Psi(x)}{dx}\right)^2\right]}dx \tag{26}$$

where $\mu(x)$ is the viscosity of water at distance x from the montmorillonite surface, μ_0 is the viscosity coefficient of the bulk water (Pa·s), f_{ve} is the viscoelectric constant (m^2/V^2), and $\Psi(x)$ is an electric potential at distance x from the montmorillonite surface (V).

The Gouy-Chapman diffuse double layer theory is applied to calculate the electric potential of near the montmorillonite surface. Since the ion distribution in the diffuse double layer obeys the Poisson–Boltzmann equation, a relation between the electric potential and ion distribution is expressed as follows:

$$\frac{d^2\Psi(x)}{dx^2} = -\frac{1}{\varepsilon_0\varepsilon_w}\sum_i z_i e c_{b,i}\exp\left(-\frac{z_i e\Psi(x)}{k_B T}\right) \tag{27}$$

where ε_0 is the vacuum permittivity (C/V/m), ε_w is a relative permittivity of solution (–), z_i is a valence of species i (–), e is the elementary charge (C), $c_{b,i}$ is a number concentration of species i in the bulk solution ($1/m^3$), k_B is the Boltzmann constant (J/K), and T is the absolute temperature (K).

Equation (27) is solved by taking a surface charge density and the potential gradient of the mid-plane between two parallel plates (Verwey & Overbeek 1948; Tachi & Yotsuji 2014).

$$\left.\frac{d\Psi(x)}{dx}\right|_{x=0} = -\frac{\sigma_0}{\varepsilon_0\varepsilon_w} = -\frac{CEC}{\varepsilon_0\varepsilon_w S}, \quad \left.\frac{d\Psi(x)}{dx}\right|_{x=\frac{X}{2}} = 0 \tag{28}$$

where σ_0 is the surface charge density of montmorillonite (C/m^2), CEC is a cation exchange capacity (C/kg), and S is the specific surface area of montmorillonite (m^2/kg)].

For the sake of simplicity, the number concentration in the bulk solution is calculated by assuming a 1:1 electrolyte solution concentration ratio obtained based on the ionic strength of equilibrium concentration with respect to Kunipia F (Na-montmorillonite; solid-to-liquid ratio: 250 g/l (Oda & Shibata 1999)), a refined bentonite commercially available from Kunimine Industries Co. Ltd, Japan, using PHREEQC (Parkhurst & Appelo 2013). Table 2 shows the parameters used for solving Equations (26)–(28).

The hydraulic conductivities vary with the changes in the ionic strength of the solution permeating the specimen caused by the changing viscosity of the water and the basal spacing (Norrish 1954). Although the ionic strength is a significant factor for the hydraulic conductivity, this paper only considers the basic case of permeation by pure water. More cases will have to be considered to clarify the effects of the ionic strength on the hydraulic conductivity.

Figure 6 shows the relation of the effective montmorillonite density and hydraulic conductivity, which is the comparison of this study with experimental data of previous studies (Suzuki *et al.* 1992; Matsumoto *et al.* 1997; Maeda *et al.* 1998; Hasegawa 2004; Butsuda *et al.* 2006; Ito *et al.* 2010a, 2010b). For Na-montmorillonite, the M&Q model of $n = 2$ and $n = 3$ is in good agreement with the experimental data of previous studies. For Na-bentonite and sand-bentonite mixtures, the M&Q model of

Table 2 | Parameters for the calculation of hydraulic conductivity

Density of water (ρ_w)	997 (kg/m^3)
Gravitational acceleration (g)	9.81 (m/s^2)
Viscosity of bulk solution (μ)	8.94×10^{-4} (Pa·s)
Vacuum permittivity (ε_0)	8.85×10^{-12} (C/V/m)
Relative permittivity of solution (ε_w)	78.5
Elementary charge (e)	1.60×10^{-19} (C)
Boltzmann constant (k_B)	1.38×10^{-23} (J/K)
Viscoelectric constant (f_{ve})	1.02×10^{-15} (m^2/V^2) (Lyklema & Overbeek 1961)
CEC of montmorillonite (CEC)	1.11×10^2 (meq/100 g) (Suzuki *et al.* 2012)
Ionic strength of solution	0.03 (mol/l)

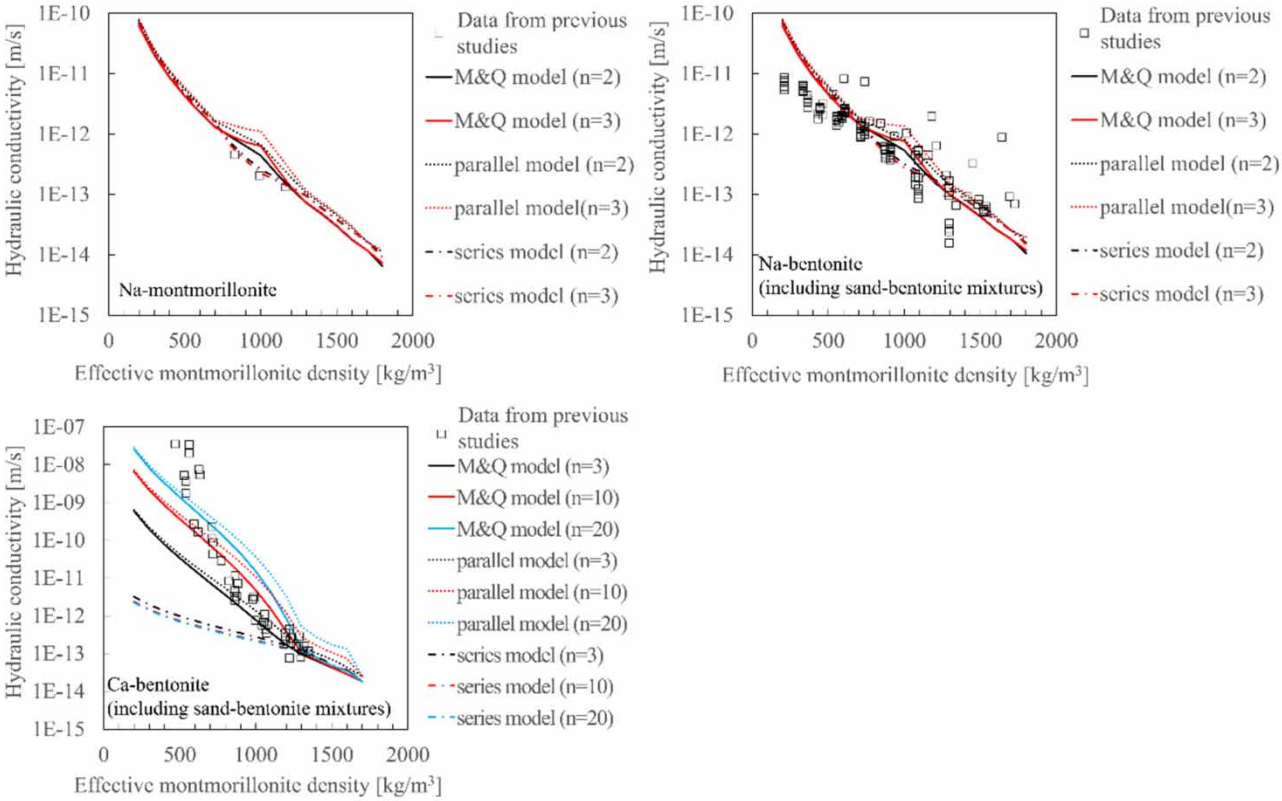

Figure 6 | Relation between the effective montmorillonite density and hydraulic conductivity.

$n = 3$ is consistent with the scattered experimental data at 500 kg/m^3 $\leq \rho_{em} \leq$ 1,500 kg/m^3. For Ca-bentonite and sand-bentonite mixtures, the M&Q model of $n = 3$–20 is in agreement with the experimental data.

The M&Q model is compared with the parallel model and the series model. The results of the M&Q model are similar to those of Na-montmorillonite and Na-bentonite (including sand-bentonite mixtures), with the exception of the densities, namely, 700 kg/m^3 $< \rho_{em} \leq$ 1,300 kg/m^3. The porosity ratio of the external pores in these densities is higher than that in other densities (Figure 7), increases sharply in the range of the mixed state of the osmotic swelling state and the 3WH state (700 kg/m^3 $< \rho_{em} <$ 1,000 kg/m^3), and decreases sharply in the range of the 3WH state only (1,000 kg/m^3 $\leq \rho_{em} \leq$ 1,300 kg/m^3). The increase of the external pores can be explained by the effect causing the decrease of the interlayer

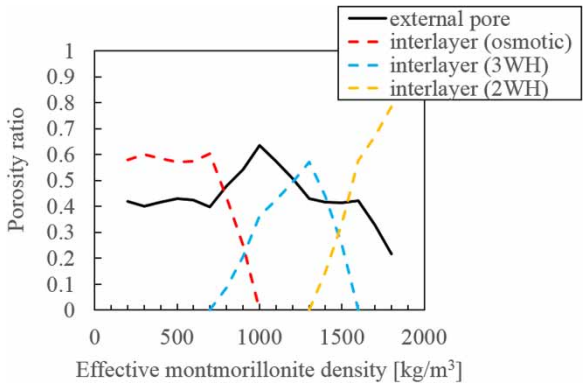

Figure 7 | Relation between the porosity ratio and effective montmorillonite density ($n = 3$).

pore width (which changes from the osmotic swelling state to the 3WH state) and is larger than the effect causing the increase in the number of stacks. The decrease of the ratio of the external pores is only affected by the increase of the number of stacks (density) because the interlayer pore width does not change at 1,000 kg/m^3 ≤ ρem ≤ 1,300 kg/m^3. Since the parallel model considers the hydraulic paths flowing through the external pores and the interlayer pores independently, the hydraulic conductivity is controlled by the large pores, that is, the external pores. In the series model, in contrast, the hydraulic conductivity is strongly affected by the small pores, that is, the interlayer pores with the 3WH state. The M&Q model is an intermediate result between the parallel model and the series model at 700 kg/m^3 < ρ_{em} ≤ 1,300 kg/m^3. The M&Q model reflects the permeability of dominant flow paths and reproduces the scattered experimental data at 500 kg/m^3 ≤ ρ_{em} ≤ 1,500 kg/m^3 for Na-bentonite. On the other hand, this model estimates far higher and far lower than the experimental data at ρ_{em} < 500 kg/m^3 and 1,500 kg/m^3 < ρ_{em}, respectively. The reason for differences between the experimental data and the model is not clear; however, it is possible that the flow paths are kept in the external pore under high-density conditions, and are prevented by particle-selves, which meant generating dead-ends, under low-density conditions.

For Ca-bentonite (including sand-bentonite mixtures), the hydraulic conductivity of the series model markedly differs from that of the experimental results at ρ_{em} < 1,000 kg/m^3, because the model result represents a harmonic mean of the external pores and the 3WH state interlayer pores. This implies that the main flow path of Ca-bentonite at ρ_{em} < 1,000 kg/m^3 is the external pores.

The scattered data on the hydraulic conductivities of Ca-bentonite (including sand-bentonite mixtures) at 600 kg/m^3 ≤ ρ_{em} indicate that the aggregation of montmorillonite particles occurs due to difference in the strength of matrix suction at compaction (Sakita *et al.* 2020). Many small pores are distributed in the external pores because montmorillonite particles are likely to be dispersed in between sand grain skeletons when the degree of saturation is high at compaction (see the schematic image in Figure 7, from Sakita *et al.* 2020). In contrast, relatively large pores are generated in the external pores because the montmorillonite particles aggregate around the sand grains when the degree of saturation is low at compaction. Ca-montmorillonite swells only up to the 3WH state in the case when the effective montmorillonite density is low. When the aggregation of montmorillonite particles around the sand grains at the low-initial degree of saturation, pores between the sand grains are not filled by Ca-montmorillonite and are created relatively large one in them. Although the M&Q models from $n = 3$–20 are in agreement with the experimental results showing >80% saturation at compaction, they are inconsistent with the <80% saturation as shown in Figure 8. The M&Q model appears to enable the estimation of the hydraulic conductivity for Ca-bentonite when the degree of saturation at compaction is high, as the model assumes a homogeneous distribution of montmorillonite particles. The M&Q model, on the other hand, does not apply when the degree of saturation at compaction is low, as the distribution of montmorillonite particles is heterogeneous due to the generated flow paths of the relatively large pores. The heterogeneous condition is a unique condition when using a Ca-bentonite-sand mixture at the low-initial degree of saturation. Therefore, the proposed model can be applied to most cases with permeation through pure water or a low-ionic strength solution.

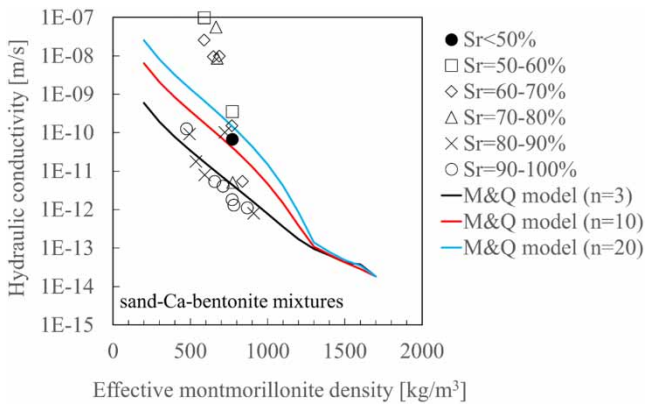

Figure 8 | Relation between the effective montmorillonite density of Ca-type bentonite mixed soil and hydraulic conductivity (degree of initial saturation, Sakita *et al.* 2020).

CONCLUSIONS

We proposed a model to demonstrate the relation between the hydraulic conductivity of bentonite and an effective montmorillonite density. Importantly, the model distinguishes between the interlayer pores of montmorillonite and the other pores (external pores), because their widths differ. We calculated the interlayer pore width from a proposed equation showing the relation between the basal spacing of montmorillonite and the effective montmorillonite density. The number of montmorillonite particle laminations in the stack was also significant as a variable required for the calculation of the external pore width. The proposed model was sufficient to estimate the hydraulic conductivity of bentonite and reproduced the difference between low-permeability and high-permeability at low-density conditions for Na- and Ca-bentonite, respectively. As the proposed model assumed a homogeneous distribution of montmorillonite particles in the specimen, however, care had to be taken to disallow application to Ca-bentonite when the saturation at compaction was low, as relatively large pores were generated due to the aggregation of the montmorillonite particles near the sand grains. The heterogeneous conditions were created by aggregation and the little swelling of Ca-montmorillonite, while the large swelling of Na-montmorillonite ensured the homogeneous condition and kept low hydraulic conductivity at low-density conditions without considering the effect of the initial degree of saturation.

DATA AVAILABILITY STATEMENT

All relevant data are included in the paper or its Supplementary Information.

CONFLICT OF INTEREST

The authors declare there is no conflict.

REFERENCES

Andrade, E. N. D. C. & Dodd, C. 1946 The effect of an electric field on the viscosity of liquids. *Proceedings of the Royal Society of London Series A* **187** (1010), 296–337.

Bolt, G. H. 1956 Physico-chemical analysis of the compressibility of pure clays. *Géotechnique* **6**, 86–93.

Butsuda, R., Komine, H., Yasuhara, K. & Murakami, S. 2006 Advancement of experimentation for measuring hydraulic conductivity of bentonite using high-pressure consolidation test apparatus. *Proceedings of Japan Society of Civil Engineers C* **62** (3), 573–578.

Childs, E. C. & Collis-George, N. 1950 The permeability of porous materials. *Proceedings of the Royal Society of London Series A* **201** (1066), 392–405.

Fink, D. H. & Thomas, G. W. 1964 X-ray studies of crystalline swelling in montmorillonites. *Soil Science Society American Proceedings* **28** (6), 747–750.

Foster, W. R., Savins, J. G. & Waite, J. M. 1954 Lattice expansion and rheological behavior relationships in water-montmorillonite systems. *Clays and Clay Minerals* **3** (1), 296–316.

Fukushima, Y. 1984 X-ray diffraction study of aqueous montmorillonite emulsions. *Clays and Clay Minerals* **32** (4), 320–326.

Gueddouda, M. K., Goual, I., Benabed, B., Taibi, S. & Aboubekr, N. 2016 Hydraulic properties of dune sand-bentonite mixtures of insulation barriers for hazardous waste facilities. *Journal of Rock Mechanics and Geotechnical Engineering* **8**, 541–550.

Hasegawa, T. 2004 *Effect of Seawater on Hydraulic Conductivity and Wetting Process of Bentonite, Civil Engineering Research Laboratory Rep. No. N04005, Central Research Institute of Electric Power Industry (in Japanese)*.

Holmboe, M., Wold, S. & Jonsson, M. 2012 Porosity investigation of compacted bentonite using XRD profile modeling. *Journal of Contaminant Hydrology* **128** (1–4), 19–32.

Ichikawa, Y., Kawamura, M., Nakano, M., Kitayama, K. & Kawamura, H. 1999 Unified molecular dynamics and homogenization analysis for bentonite behavior: current results and future possibilities. *Engineering Geology* **54** (1–2), 21–31.

Iida, Y., Yamaguchi, T. & Tanaka, T. 2011 Experimental and modeling study on diffusion of selenium under variable bentonite content and porewater salinity. *Journal of Nuclear Science and Technology* **48** (8), 1170–1183.

Ito, H., Miyasaka, N., Kozaki, T. & Sato, S. 2010a A study on hydraulic properties of compacted Fe(III)-montmorillonite. *Journal of Nuclear Science and Technology* **47** (11), 1005–1010.

Ito, Y., Niwase, K., Kaneko, T., Chichimatsu, M. & Nakakoshi, A. 2010b Study of design method for low bentonite ratio sand-bentonite mixtures based on changing in long-term state. In *Japan Society of Civil Engineers 2010 Annual Meeting*, Sapporo, Japan, pp. 33–34 (in Japanese).

Kobayashi, I., Owada, H., Ishii, T. & Iizuka, A. 2017 Evaluation of specific surface area of bentonite-engineered barriers for Kozeny-Carman law. *Soils and Foundations* **57** (5), 683–697.

Kohno, M. 2021 Swelling-pressure and hydraulic conductivity of compacted clays focusing on the clay-mineral type. *Journal of the Society of Materials Science, Japan* **70** (3), 272–278 (in Japanese).

Komine, H. 2008 Theoretical equations on hydraulic conductivities of bentonite-based buffer and backfill for underground disposal of radioactive wastes. *Journal of Geotechnical and Geoenvironmental Engineering* **134** (4), 497–508.

Kozaki, T., Fujishima, A., Sato, S. & Ohashi, H. 1998 Self-diffusion of sodium ions in compacted sodium montmorillonite. *Nuclear Technology* **121** (1), 63–69.

Lee, J. M. & Shackelford, C. D. 2005 Impact of bentonite quality on hydraulic conductivity of geosynthetic clay liners. *Journal of Geotechnical and Geoenvironmental Engineering* **131** (1), 64–77.

Low, P. F. 1976 Viscosity of interlayer water in montmorillonite. *Soil Science Society of America Journal* **40** (4), 500–505.

Lyklema, J. & Overbeek, J. T. G. 1961 On the interpretation of electrokinetic potentials. *Journal of Colloid Science* **16**, 501–512.

Maeda, M., Tanai, K., Ito, M., Mihara, M. & Tanaka, M. 1998 *Mechanical Properties of the Ca Exchanged Ca Bentonite; Swelling Pressure, Hydraulic Conductivity, Compressive Strength and Elastic Modulus*, PNC TN8410 98-021, Power Reactor Nuclear Fuel Development Corporation, Japan (in Japanese).

Malusis, M. A., Evans, J. C. & Yeom, S. 2011 Hydraulic conductivity of model soil-bentonite backfills subjected to wet-dry cycling. *Canadian Geotechnical Journal* **48** (8), 198–211.

Marshall, T. J. 1958 A relation between permeability and size distribution of pores. *Journal of Soil Science* **9** (1), 1–8.

Matsumoto, K., Kanno, T., Fujita, T. & Suzuki, H. 1997 *Hydraulic Properties of Saturated Buffer Material*, PNC TN8410 97-296, Power Reactor Nuclear Fuel Development Corporation, Japan (in Japanese).

Matusewicz, M., Pirkkalainen, K., Liljeström, V., Suuronen, J. P., Root, A., Muurinen, A., Serimaa, R. & Olin, M. 2013 Microstructural investigation of calcium montmorillonite. *Clay Minerals* **48** (2), 267–276.

Meer, S. R. & Benson, C. H. 2007 Hydraulic conductivity of geosynthetic clay liners exhumed from landfill final covers. *Journal of Geotechnical and Geoenvironmental Engineering* **133** (5), 550–563.

Millington, R. J. & Quirk, J. P. 1961 Permeability of porous solids. *Transactions of the Faraday Society* **57**, 1200–1207.

Nahin, K. T. K., Basak, R. & Alam, R. 2019 Groundwater vulnerability assessment with DRASTIC index method in the salinity-affected Southwest Coastal Region of Bangladesh: a case study in Bagerhat Sadar, Fakirhat and Rampal. *Earth Systems and Environment* **4**, 183–195.

Norrish, K. 1954 Manner of swelling of montmorillonite. *Nature* **173** (4397), 256–257.

Oda, C. & Shibata, M. 1999 *Modelling and Experimental Studies on Bentonite-Water Interaction*. JNC TN8400 99-032, Japan Nuclear Cycle Development Institute, Japan (in Japanese).

Park, D. & Oh, J. 2018 Permeation grouting for remediation of dam cores. *Engineering Geology* **233**, 63–75.

Parkhurst, D. L. & Appelo, C. A. J. 2013 *Description of Input and Examples for PHREEQC Version 3 – A Computer Program for Speciation, Batch-Reaction One-Dimensional Transport, and Inverse Geochemical Calculations*. U.S. Geological Survey, Denver.

Pusch, R., Karnland, O. & Hökmark, H. 1990 *GMM – A General Microstructural Model for Quantitative Studies of Smectite Clays, SKB Technical Report 90-43*. Swedish Nuclear Fuel and Waste Management Co., Sweden.

Ren, X., Zhao, Y., Deng, Q., Kang, J., Li, D. & Wang, D. 2016 A relation of hydraulic conductivity – void ratio for soils based on Kozeny-Carman equation. *Engineering Geology* **213** (4), 89–97.

Sakita, T., Komine, H., Yamada, A., Wang, H. & Goto, S. 2020 Influence of bentonite type and producing method on hydraulic conductivity of sand-bentonite mixture. *E3S Web of Conferences* **205**, 1–6.

Santos, R. A. & Esquivel, E. R. 2018 Saturated anisotropic hydraulic conductivity of a compacted lateritic soil. *Journal of Rock Mechanics and Geotechnical Engineering* **10** (5), 986–991.

Sato, H. & Suzuki, S. 2003 Fundamental study on the effect of an orientation of clay particles on diffusion pathway in compacted bentonite. *Applied Clay Science* **23**, 51–60.

Sidharan, A. & Choudhury, D. 2008 Computation of hydraulic conductivity of montmorillonitic clays by diffuse double layer theory. *International Journal of Geotechnical Engineering* **1**, 1–10.

Suzuki, H., Shibata, M., Yamagata, J., Hirose, I. & Terakado, K. 1992 Experiment for Characteristics of Buffer Material (1), PNC TN8410 92-057, PNC TN8410 92-057, Power Reactor Nuclear Fuel Development Corporation, Japan.

Suzuki, S., Fujishima, A., Ueno, K., Ichikawa, Y., Kawamura, K., Fujii, N., Shibata, M., Sato, H. & Kitayama, K. 2001 Microstructural modeling of compacted sodium-bentonite and application of unified molecular dynamics/homogenization analysis for diffusion process. *Nendo Kagaku* **41** (2), 43–57 (in Japanese).

Suzuki, S., Sato, H., Ishidera, T. & Fujii, N. 2004 Study on anisotropy of effective diffusion coefficient and activation energy for deuterated water in compacted sodium bentonite. *Journal of Contaminant Hydrology* **68** (1–2), 23–37.

Suzuki, K., Sato, T. & Yoneda, T. 2012 Factors affecting to the viscosity of montmorillonite/water suspension, 2. relationship between aspect ratio of montmorillonite particles and viscosity of aqueous suspensions. *Nendo Kagaku* **50** (3), 162–174 (in Japanese).

Tachi, Y. & Yotsuji, K. 2014 Diffusion and sorption of Cs^+, Na^+, I^- and HTO in compacted sodium montmorillonite as a function of porewater salinity: integrated sorption and diffusion model. *Geochimica et Cosmochimica Acta* **132**, 75–93.

Takahashi, H. & Tachi, Y. 2019 3D-microstructure analysis of compacted Na- and Cs-montmorillonites with nanofocus X-ray computed tomography and correlation with macroscopic transport properties. *Applied Clay Science* **168**, 211–222.

Tanaka, Y., Hasegawa, T. & Nakamura, K. 2009 Modeling hydraulic conductivity and swelling pressure of several compacted bentonites affected by salinity of water. *Proceedings of Japan Society of Civil Engineers C* **65** (1), 66–84 (in Japanese).

Tournassat, C., Neaman, A., Villiéras, F., Bosbach, D. & Charlet, L. 2003 Nanomorphology of montmorillonite particles: estimation of the clay edge sorption site density by low-pressure gas adsorption and AFM observations. *American Mineralogist* **88** (11–12), 1989–1995.

Verwey, E. J. W. & Overbeek, J. T. G. 1948 *Theory of the Stability of Lyophobic Colloids*. Elsevier, Amsterdam.

Wang, H., Komine, H. & Gotoh, K. 2021 A swelling pressure cell for X-ray diffraction test. *Géotechnique*, Ahead of print, 1–12.

Zhang, Z. Z. & Low, P. F. 1989 Relation between the heat of immersion and the initial water content of Li-, Na-, and K-montmorillonite. *Journal of Colloid and Interface Science* **133** (2), 461–472.

First received 27 January 2022; accepted in revised form 19 August 2022. Available online 23 September 2022